Materials Science & Engineering A 691 (2017) 203–210

Contents lists available at ScienceDirect

Materials Science & Engineering A

journal homepage: www.elsevier.com/locate/msea

Mechanical behavior of rare-earth orthophosphates near the monazite/xenotime boundary characterized by nanoindentation

Taylor M. Wilkinson[a], Dong Wu[a], Matthew A. Musselman[a], Nan Li[b], Nathan Mara[b,c], Corinne E. Packard[a,*]

[a] Metallurgical and Materials Engineering Department, Colorado School of Mines, Golden, CO 80401, USA
[b] Center for Integrated Nanotechnologies, Los Alamos National Laboratory, Los Alamos, NM 87545, USA
[c] Institute for Materials Science, Los Alamos National Laboratory, Los Alamos, NM 87545 USA

ARTICLE INFO

Keywords:
Nanoindentation
Mechanical characterization
Ceramics
Phase transformation
Twinning

ABSTRACT

Low elastic modulus and hardness, as well as anomalous indentation behavior, have been observed during indentation of xenotime rare-earth orthophosphate ceramics ($REPO_4$s) with compositions near the monazite/xenotime phase boundary. Pressure-induced phase transformation has been identified as a potential cause for both observations. This study comprehensively characterizes the mechanical properties and indentation behavior of four elemental $REPO_4$ materials ($EuPO_4$, $GdPO_4$, $TbPO_4$, and $DyPO_4$) that span the monazite/xenotime phase boundary using *ex situ* nanoindentation for a range of loading rates and indentation depths. *In situ* nanoindentation within a SEM was used to correlate discrete load-depth behavior to the development of surface features. Anomalous, elbow-type behavior was not restricted to xenotimes, but occurred in all four materials; thus we concluded that the presence of an elbow in the indentation data was not a unique identifier of phase transformation in rare-earth orthophosphates. Furthermore, it was shown that the elastic modulus of each of these compositions approached the value predicted by simulations and hardness was consistently above 5 GPa, provided that the samples were processed to nearly full density.

1. Introduction

Excellent resistance to chemical and thermal degradation [1,2] have made rare-earth orthophosphates ($REPO_4$s) a promising class of materials for toughness-enhancing fiber coatings in oxide-oxide ceramic matrix composites (CMCs) [3,4], as was first demonstrated with $LaPO_4$ by Davis et al. [3] Experimentation by Hay et al. with the solid-solution rare-earth orthophosphate $(Gd_{0.4}Dy_{0.6})PO_4$ was successful in achieving favorable reductions in fiber sliding stresses compared to $LaPO_4$ [4]. The solid-solution composition was chosen to capture the benefits of $LaPO_4$ while potentially imparting transformation plasticity to the system by reducing the effective rare-earth radius sufficiently to stabilize a xenotime structure, which can undergo pressure-induced phase transformation [4]. The xenotime structure has a tetragonal crystal system, with space group $I41/amd$ (Z=4), and is the equilibrium structure at ambient pressure and temperature for $REPO_4$s with rare-earth elements with atomic numbers 65–71 [1,2,5,6]. Smaller rare-earth elements with atomic numbers 57–64, inclusive of lanthanum, prefer the monazite structure, which is monoclinic with space group $P21/n$ (Z=4) [1,2,5,6]. Post-mortem transmission electron microscopy (TEM) of $(Gd_{0.4}Dy_{0.6})PO_4$ following fiber sliding confirmed the presence of regions of transformed materials in the monazite structure as well as anhydrite (space group Amma, Z=4), supporting the hypothesis that transformation plasticity had occurred in the system [4].

Solid-solution $Gd_xDy_{(1-x)}PO_4$ (x=0.4–0.6) materials and elemental $TbPO_4$ were additionally prepared as polycrystalline monoliths to further elucidate the micromechanical behavior of the materials [5]. In pioneer nanoindentation testing of these materials, Hay et al. reported that the solid-solution materials exhibited low indentation moduli (51–120 GPa) and hardnesses (2.1–6.1 GPa), as well as anomalous indentation behavior in the form of an elbow during unloading [5]. A number of studies using various techniques for experimental characterization [4,5,7–10] and theoretical modeling including both chemical bond theory [11] and *ab initio* quantum chemistry [12] have reported modulus values ~100 GPa higher than values acquired through nanoindentation [5] for $REPO_4$ compositions near the monazite/xenotime border. For example, Hay et al. reported the indentation modulus of xenotime $TbPO_4$ to be 44 GPa (converted to a bulk modulus using a Poisson's ratio of 0.29 [13] – 33.3 GPa) [5]; whereas, *ab initio* quantum chemistry calculations showed a bulk

* Corresponding author.
E-mail address: cpackard@mines.edu (C.E. Packard).

http://dx.doi.org/10.1016/j.msea.2017.03.041
Received 1 February 2017; Received in revised form 8 March 2017; Accepted 9 March 2017
Available online 12 March 2017

modulus value in the range of ~140 GPa [11] for $TbPO_4$.

Low modulus and hardness values were accompanied by dramatic changes in the slope of the load-depth data during the unloading phase of indentation [5], which is commonly referred to as an 'elbow' [14]. *Ex situ* TEM of an indentation site in $TbPO_4$ showed evidence of a small grain of monazite within a xenotime matrix [5]. On the basis of this evidence, it was suggested that phase transformation during indentation might be responsible for both the low mechanical property values and the elbows in the load-depth data [5]. Phase transformation has been shown to cause elbows, as studies on silicon [14,15] and shape memory alloys [16] have shown; however, elbows can also result in systems where no phase transformation has occurred, for instance, *via* movement of twin boundaries in martensitic NiTi [17]. Elbow-type unloading behavior in single crystal and polycrystalline $GdPO_4$ (monazite) and evidence for a twinning-based ferroelastic mechanism were recently reported by a subset of the present authors in Ref. [18].

This study cataloged the mechanical properties and indentation behavior of the four elemental $REPO_4$ materials ($EuPO_4$, $GdPO_4$, $TbPO_4$, and $DyPO_4$) that span the monazite/xenotime phase boundary. Large data sets were collected using *ex situ* nanoindentation for a range of loading rates and indentation depths. Reduced elastic modulus and hardness were characterized for each composition and compared to previously reported mechanical properties. Nanoindentation load-depth data was analyzed to identify the frequency of observed discontinuities during unloading. *In situ* nanoindentation within a SEM was used to correlate discrete load-depth behavior to the development of surface features.

2. Experimental procedure

Four $REPO_4$s ($EuPO_4$, $GdPO_4$, $TbPO_4$, and $DyPO_4$) were synthesized in separate batches at ambient temperature by direct precipitation from rare-earth nitrate precursors following Boakye et al. (see Eq. (1)) [1].

$$RE(NO_3)_3 + H_3PO_4 \rightarrow REPO_4 + 3HNO_3 \quad (1)$$

First, the rare-earth nitrates (99.9% purity, Sigma Aldrich, St. Louis, MO) were dissolved in deionized water, and a solution of phosphoric acid diluted with deionized water was prepared to achieve equivalent 1:1 M ratio of rare-earth nitrate to phosphoric acid. Then, the phosphoric acid solution was added to the nitrate solution while stirring the contents, and the $REPO_4$ precipitation began to occur shortly (in about 15 s). After that, 50 mL of 30% NH_4OH was added to the mixture to achieve a basic solution (pH of ~10) to increase the precipitation rate. The precipitates were collected by filtering the resultant mixture and dried in air at room temperature for 48 h.

$EuPO_4$, $GdPO_4$, and $DyPO_4$ powders were ball milled for 24 h in ethanol using zirconia media, calcined at 1200 °C for two hours, ball-milled again for 24 h, pressed into green state at 50 MPa, and finally sintered for two hours at 1500 °C into polycrystalline pellets. Powder diffraction using a PANalytical PW3040 X-ray Diffractometer (Almelo, Netherlands) confirmed crystal structure and phase purity before and after sintering, with both $EuPO_4$ and $GdPO_4$ matching well to monazite and the peaks of $DyPO_4$ corresponding to xenotime.

A fully dense $TbPO_4$ pellet was much more difficult to obtain; multiple processing iterations (including changing sintering temperature, changing sintering time, and excluding one or both ball mill steps as well as the calcination step) did not result in a fully dense sample of $TbPO_4$. Thus, hot pressing in a Thermal Technologies 610 G-25T press (Santa Rosa, CA) using a graphite die was employed. Amorphous $TbPO_4$ was calcined at 1200 °C for two hours and then processed using a 3 °C/minute ramp rate up to 1300 °C, three hour hold, and 3 °C/minute cooling rate to room temperature. Simultaneously, the pressure was held steady during the temperature ramp at 10.5 MPa, increased to 40 MPa during the temperature hold, and then brought back to a constant 10.5 MPa during cooling. X-ray diffraction was used to confirm single-phase xenotime structure in the $TbPO_4$ pellet.

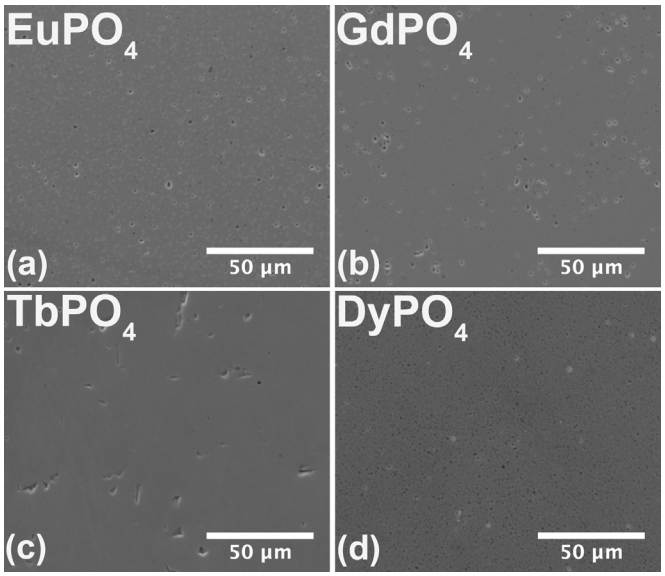

Fig. 1. SEM images of the polished samples' surfaces – (a) $EuPO_4$, (b) $GdPO_4$, (c) $TbPO_4$, and (d) $DyPO_4$. Density measurements for each of the samples yield > 98% theoretical density.

Pellets were mounted in epoxy and polished using standard ceramographic techniques to create a smooth surface for indentation testing; the pellets had less than five nanometers of surface roughness (Rq) over an area of 25 μm^2 which was verified using the scanning probe feature of the nanoindenter. An FEI Quanta 600i environmental scanning electron microscope (FEI – Hillsborro, OR) (SEM), in conjunction with ImageJ image processing software (National Institute of Health, Bethesda, MD), was used to analyze the polished surface of each $REPO_4$ pellet to conduct density measurements. The surface of each pellet was imaged in ten different locations at 1000x magnification. A gray-scale intensity threshold was applied to each image to isolate pores, pore area was summed, and an area fraction was calculated from which the porosity was inferred [19]. The average density and its standard deviation were calculated for each of the samples, showing that each pellet was near full theoretical density: $EuPO_4$=99.3 ± 0.1%, $GdPO_4$=98.7 ± 0.7%, $TbPO_4$=98.5 ± 0.6% and $DyPO_4$=99.2 ± 0.5%, where the theoretical densities were calculated as 5.82, 6.00, 5.79, and 5.95 g/cm^3, respectively, based on crystallographic data provided by Ni et al. [20] Fig. 1 shows a collection of representative SEM micrographs of the surface area for each sample.

Ex situ indentation tests were performed on the $REPO_4$ samples using a Hysitron TI-950 TriboIndenter (Minneapolis, MN) equipped with Berkovich tips and two different loading heads: ≤30 nN to 10 mN and 10 mN to 500 mN. For the lower load range, 100 indentations with a 10 mN peak load were performed on each material at loading rates that varied over three orders of magnitude (0.33 mN/s, 3.33 mN/s, and 33.3 mN/s). In another set of tests, peak load was varied using a constant loading rate of 3.33 mN/s, with five indentations at peak loads of 2.5 mN, 5 mN, 10 mN, and 20 mN to 400 mN in 10 mN increments. All the load-displacement curves for *ex situ* indentation tests were analyzed using the Oliver-Pharr method to determine reduced elastic modulus and hardness [21]. Each 10-mN load-depth (P-h) curve was analyzed manually to identify anomalous unloading behavior. A custom procedure was created for standardizing the detection of a change in the unloading slope that is characteristic of elbow-type behavior. The unloading data of each indentation test was run through a smoothing filter, and then the instantaneous unloading slope, $\frac{dP}{dh}$, was calculated. The logarithm of ($\frac{dP}{dh}$) was plotted *versus* time to highlight slope changes, and an empirical threshold of > 10% change in $\log(\frac{dP}{dh})$ was used to assign elbow-type behavior.

A limited number of *in situ* nanoindentation tests were also conducted to allow for alignment of the load-depth response with the deformation of the material. Three of the four materials, $EuPO_4$, $GdPO_4$, and $TbPO_4$, were characterized using an *in situ* Hysitron PI-85 PicoIndenter (Minneapolis, MN) and an FEI Magellan^3 400 (Hillsboro, OR) SEM at the Center for Integrated Nanotechnologies at Los Alamos National Laboratory (Los Alamos, NM). In total, ten indentation tests with peak loads of 20 mN were performed on each of the materials using a cube corner tip and a 0.33 mN/s loading rate. Nanoindentation data was analyzed using the procedures outlined above. Additionally, each load-depth data set was correlated to the corresponding time series of micrographs.

3. Results and discussion

3.1. Mechanical behavior

A variety of behaviors were observed in the load-displacement curves during indentation, including pop-ins (discrete displacement jumps into the material during loading), elbows, and pop-outs (discrete displacement of the tip out of the material during unloading). Pop-ins were observed in the loading portions of all experiments at all loading rates in all four materials, which indicated that these features are universal and not restricted to either monazite or xenotime compositions; representative load-depth data showing pop-ins are shown in Fig. 2(a) and (b). Pop-ins have been commonly observed in many materials, and result from a variety of deformation mechanisms. In silicon carbide and sapphire, pop-ins have been associated with fracture of the material around and below the indentation site [22,23]. Pop-ins also result from dislocation nucleation and slip to the surface in materials including silicon carbide [24], sapphire [25], and MgO [26], making it difficult to assign the behavior to a certain deformation mechanism without additional characterization. The observation of pop-ins in the four elemental $REPO_4$ materials examined here is consistent with prior reports on $GdPO_4$, $TbPO_4$, and $DyPO_4$ [5,18].

Fig. 2 additionally illustrates the two types of anomalous behavior that were observed during testing: elbow-type behavior (a) and pop-out (b). In Fig. 2(a), a black arrow was used to highlight the area of interest, where the slope changed to create an elbow in the data. Fig. 2(b) includes an enlarged view of the pop-out in the inset figure, with a discrete displacement jump of 1–2 nm as the tip was rapidly and discontinuously pushed out of the material during the unloading process. Elbows were previously observed in several pure ($GdPO_4$, $DyPO_4$, and $TbPO_4$) and several solid-solution ($(Gd_xDy_{x-1})PO_4$ where x=0.4 – 0.6) polycrystalline $REPO_4$ materials [5], but the presence or absence of pop-outs was not noted. Elbows have also been observed in a $GdPO_4$ single crystal [18]. $REPO_4$s are not alone in exhibiting pop-out and elbow-type behaviors; silicon has also shown anomalous behavior in the unloading portions of the load-displacement curves as a result of silicon-I undergoing a pressure-induced transformation upon loading to metallic silicon-II, and further transforming upon unloading to a specific structure depending on the indenter angle, indentation load, and/or indentation rate [14,15,23]. Additionally, NiTi shape memory alloys produce both elbows and pop-outs, depending on the alloy and testing parameters [16,27].

Fig. 3 shows a stacked bar chart highlighting the observation frequency of pop-outs, elbows, and normal unloading (does not exhibit elbow or pop-out) from 1200 indentation tests across the four materials. Table 1 in the Supplemental material provides the information from Fig. 3 numerically. The elbow phenomenon was observed frequently, appearing in 24–59% of the data sets across the $REPO_4$ compositions studied here. Both monazite compositions, which do not undergo phase transformation under pressure [9], exhibited elbows at roughly the same rate as the xenotime compositions, which can undergo phase transformation under pressure in hydrostatic conditions [9,28] and in complex multiaxial stress fields associated with indentation [5,6]. No other consistent, statistically significant trends in composition were observed. The observation of elbows in $EuPO_4$ supported and expanded the conclusion of Wilkinson et al. [18] that elbows cannot be used to diagnose phase transformation in $REPO_4$s because monazite compositions exhibited the behavior as well. Elbows were not observed in every test, which may have one or more explanations; local grain orientation and microstructure in the polycrystalline material may have impacted ease of phase transformation (for xenotimes) or twinning (both structures) and/or hindered the movement of twin or phase boundaries responsible for recovery on unloading, depending on plastic deformation accumulated on loading. The frequency of elbow observation had no statistically significant loading-rate dependence across the three orders of magnitude in loading rate explored here. Rate independence was suggestive of a large activation energy for the controlling deformation mechanism operating in the athermal, stress-biased limit. In $GdPO_4$ and $EuPO_4$, the observed lack of rate dependence was consistent with the athermal nature of twinning [29]. The potential for a twinning mechanism to contribute at least partially to the observed recovery in xenotimes should not be ruled out at this point as deformation by twinning has been observed in xenotime YPO_4 [30], and naturally occurring

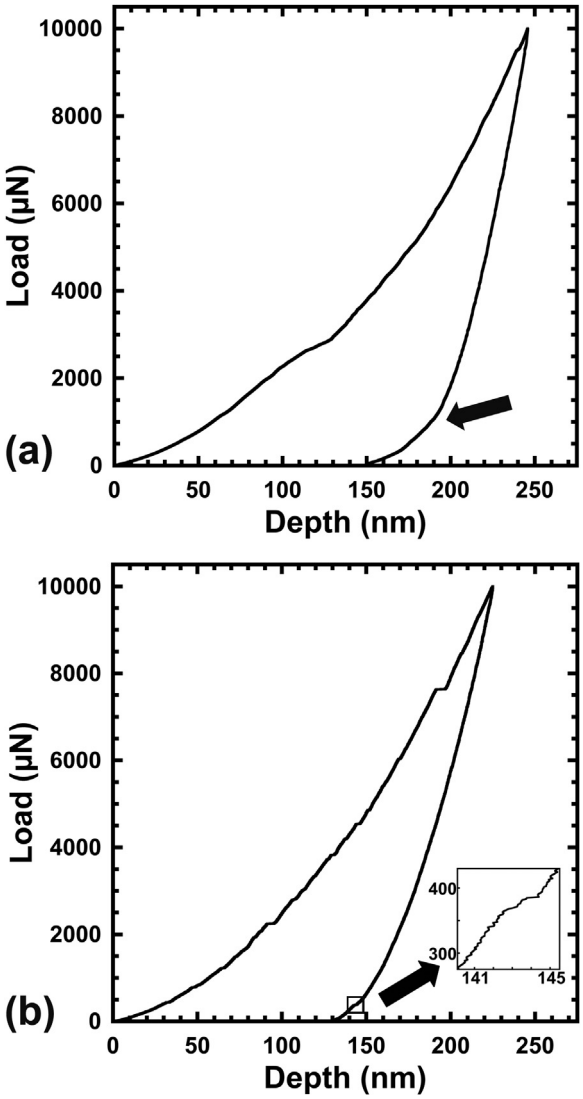

Fig. 2. Representative nanoindentation data from rare-earth orthophosphates showing pop-ins and other behavior including (a) an elbow during unloading, and (b) a pop-out upon unloading.

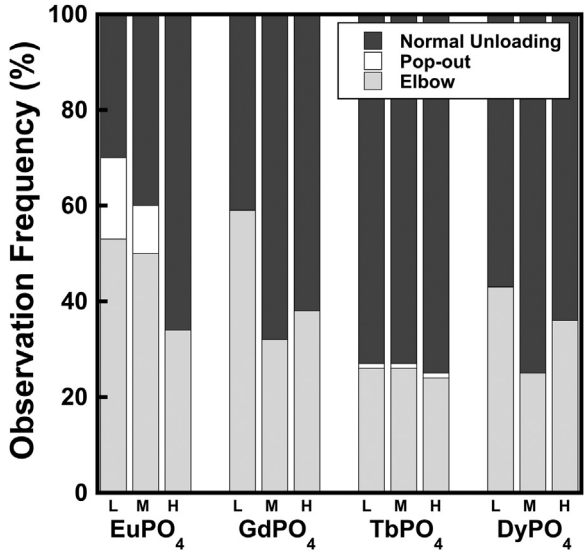

Fig. 3. Frequency of normal unloading, pop-outs, and elbows, for each material and loading rate (L – low loading rate, M – medium loading rate, and H – high loading rate). Pop-outs are only seen in $EuPO_4$ and $TbPO_4$.

xenotimes [31]. Twinning has also been observed in anhydrite $(Gd_{0.4}Dy_{0.6})PO_4$ [6], one of the xenotime's high-pressure phases, following deformation by indentation.

Pop-out features were relatively rare events. Pop-outs occurred most frequently in monazite $EuPO_4$ at the slowest loading rate, but still represented less than 20% of the total tests. Xenotime $TbPO_4$ exhibited pop-outs as well, with one occurrence in each of the three loading-rate datasets. Pop-outs were not observed in $GdPO_4$ or $DyPO_4$, nor were they noted in previous studies [5,18]. The rare nature of these events within the sample size precluded detailed conclusions about the mechanism-, material-, or rate-dependence of pop-outs. The directionality of the behavior (tip is pushed out by material recovery) is the same for pop-outs as elbows, thus the same mechanism could be responsible for the two phenomena, with the competition between the driving force and obstruction potentially determining whether recovery was discrete (pop-out) or continuous (elbow).

In situ nanoindentation within an SEM was used to examine the correspondence of mechanical behavior observed in the load-depth data with the development of surface features. Testing with a cube corner tip *in situ* permitted a wider field of view in observing the surface, compared to the Berkovich geometry employed in the rest of this work. In preparation for the required change in tip geometry for the *in situ* testing, a set of 75 indentations were completed using a cube corner tip at the three various loading rates (0.33, 3.33, and 33.3 mN/s) in each of the four materials. Data provided in Table 2 in the Supplemental material confirmed that the frequency of each behavior (pop-ins, elbows, pop-outs, normal unloading) obtained with a cube corner tip showed similar trends to that in Fig. 3.

Videos of representative *in situ* indentations for $EuPO_4$, $GdPO_4$, and $TbPO_4$ are available in the Supplemental information section, along with time-based annotations correlating load-depth behavior with the development of features observed by SEM. The behavior of $GdPO_4$ is summarized here with a selection of micrographs in Fig. 4, which is a 4-part figure comprised of representative *in situ* indentation load-depth data from $GdPO_4$, (a), and SEM micrographs (b,c,d) corresponding to points in time indicated by arrows in (a). Fig. 4(b) shows an initial image of the sample surface before the occurrence of the large pop-in marked in the load-depth curve in Fig. 4(a). As loading continued, a large pop-in occurred, corresponding to an ejection of material to the right of the indenter tip (red arrow) as seen in Fig. 4(c). No further evolution of the surface was observed during unloading. The final micrograph, 4(d), shows the sample surface after the extraction of the tip. A pile-up of material as well as several cracks surrounded the indentation site on the sample surface. A series of parallel steps, likely corresponding to slip lines, were also observed to the right of the residual indent, as highlighted by a red arrow in Fig. 4(d). Slip lines are not commonly observed in brittle solids due to their propensity to fail by fracture before appreciable dislocation activity occurs; however, the confinement created by indentation testing can allow their development, as shown by Ghosh et al. and Huang et al. in ZrB_2 and ultrafine grained alumina, respectively [32,33]. Slip system orientation within grains can allow the development of slip lines; however, distribution of strain within and between grains with non-favorable orientations ultimately lead to a crack-tip opening and failure [32]. In the case of the indentation of $GdPO_4$, slip lines were accompanied by observations of fracture and the ejection of material from the sample surface, with all visible events occurring during loading. These behaviors were quite different from those of silicon, which showed extrusion of material during unloading as a result of the phase transformation [14]. No surface evolution, material extrusion, or ejection was observed during unloading in any of the *in situ* testing on $EuPO_4$, $GdPO_4$, and $TbPO_4$. Load-depth behavior and surface feature development were similar in $EuPO_4$ and $TbPO_4$ to that seen in $GdPO_4$, except that slip lines were not observed.

3.2. Mechanical properties

Hardness and elastic modulus can be readily extracted from the load-displacement curves of the indentation tests following Oliver-Pharr analysis, yet it is necessary to first investigate the influence of the anomalous unloading events (e.g. elbows and pop-outs) on the measurement of mechanical properties. Hence, both the reduced modulus and hardness values were calculated based on the 20–95% of the unloading data for each test. Tests showing elbow or pop-out were grouped as 'anomalous unloading' and compared to tests that exhibited normal unloading. Fig. 5 shows the average reduced elastic modulus (Fig. 5(a)) and average hardness (Fig. 5(b)) for the four materials at the 3.33-mN/s loading rate and 10-mN peak load for normal and anomalous unloading. Vertical error bars represent the standard deviation. Only the indentation tests with a 3.33-mN/s loading rate and 10-mN peak load are shown for brevity, as all loading rates had similar results. No statistically significant difference was observed between the normal unloading and anomalous unloading groups, as almost all of the elbows and pop-outs are located in the lower 20% portion of the unloading curve, which is below the load range typically included in analysis. Thus, the data with anomalous and normal unloading behavior were analyzed together as one group for the remainder of this paper. All four materials had reduced elastic moduli in the range of 150–180 GPa. Hardnesses for all materials exceeded 5 GPa, with monazite compositions being slightly harder than xenotimes. For comparison, Hay et al. reported a range of average reduced moduli and hardnesses for $GdPO_4$ (Er=194–199 GPa, H=6.0–7.8 GPa), $TbPO_4$ (Er=44–48 GPa, H=0.9–1.3 GPa), and $DyPO_4$ (Er=119–127 GPa, H=3.2–4.6 GPa) [5]; the modulus value for $GdPO_4$ was found to be slightly higher than the value in this study, however, the properties of the xenotime materials were shown to be substantially lower than the values found here (Fig. 6).

Broader comparison of elastic modulus results collected using other experimental and theoretical techniques was conducted by converting to bulk modulus. The present study, as well as Hay et al. [5], used sintered polycrystalline compacts and reported reduced (indentation) modulus. Reduced elastic moduli acquired from indentation tests were converted to Young's modulus (E) according to

$$\frac{1}{E_r} = \frac{1-\nu^2}{E} + \frac{1-\nu_i^2}{E_i} \quad (2)$$

where E_r is the measured reduced elastic modulus, E_i is the Young's

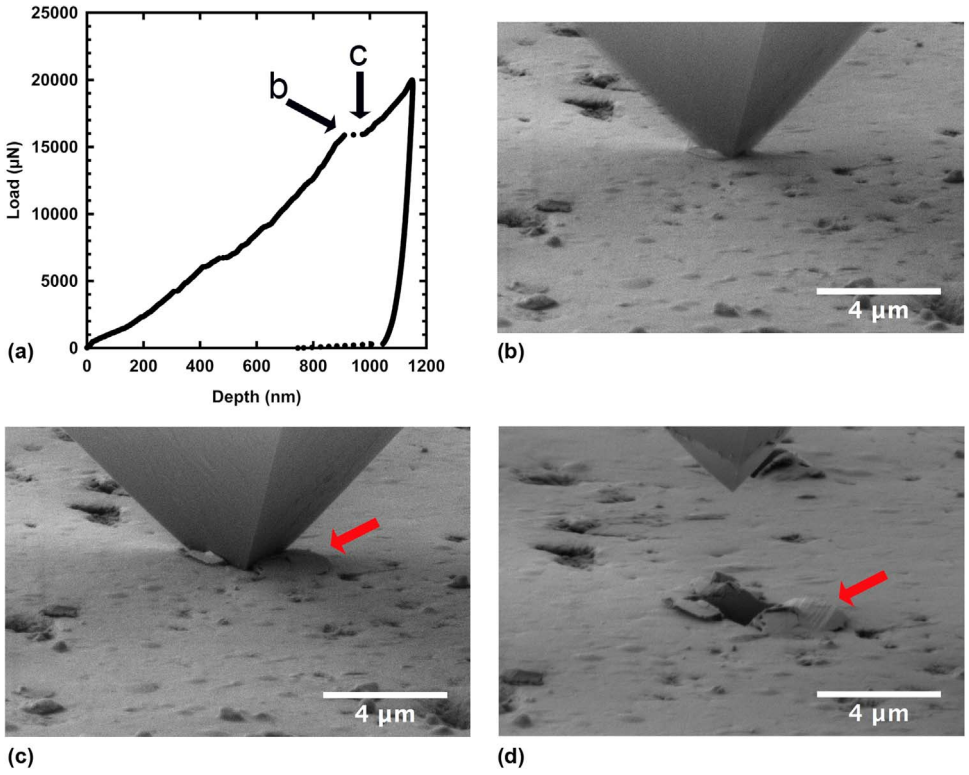

Fig. 4. $GdPO_4$ *in situ* testing: load-depth data (a) and SEM micrographs of points before pop-in (b), following pop-in showing ejection of material to the right of the indenter tip (c), and following extraction of the tip (d) where an arrow highlights slip lines in the pile-up.

modulus of the diamond indenter tip, ν_i is Poisson's ratio for diamond, ν is Poisson's ratio for the material under test, and E is Young's modulus for the material under test. The Poisson's ratio is set to 0.29 based on Feng et al. [13] for all conversions. Young's modulus was reported by Kowalski et al. using *ab initio* quantum chemistry of all four of the $REPO_4$s tested here [12], as well as Perriere et al. and Du et al., who used ultrasonic wave velocities to measure $EuPO_4$ [7,10] and $GdPO_4$ [7] powders. Young's modulus was converted to bulk modulus, B, as

$$B = \frac{E}{3(1-2\upsilon)} \tag{3}$$

where E is Young's modulus and ν is Poison's ratio (set to 0.29). Bulk modulus was reported directly by Li et al., using the computational method of chemical bond theory of dielectric description for all four $REPO_4$s [11], as well as Lacomba-Perales et al. and Heffernan et al., using diamond anvil cell compression for $EuPO_4$ and $GdPO_4$ single crystal chips [9] and a $GdPO_4$ single crystal chip [8], respectively, to determine bulk modulus.

It has been suggested that the modulus of monazite $REPO_4$s should increase very slightly with the decrease of radii values [7] and corresponding decreases in interatomic distances have been observed [2]; however, this specific trend could not be discerned for our data set given the variation in the experimental data. It was found that the values measured in the present study largely agree with those that are acquired computationally [11] and the majority of those measured experimentally [7–10], excepting the xenotime data provided by Hay et al. [5] Hay et al., as well as other researchers [34,35], have noted difficulty in densifying xenotime specimens [5]. Modulus is strongly dependent on porosity [36], thus we suspected that the deviations between data sets were attributable to the differences in density, as opposed to originating from phase transformation. Data presented in Fig. 5 supported this theory, by showing that the presence or absence of anomalous unloading does not substantial impact property measurements in dense samples.

In addition to differences in modulus, our study showed substantially higher hardness values for xenotimes compared to Ref [5]. Differences in indention depth and loading rate can have some impact on hardness values in other systems, so the impact of these parameters on hardness in $REPO_4$s was examined in more detail. Tests were conducted from 2.5 to 400 mN and hardness values were plotted as a function of maximum indentation depth in Fig. 7. Error bars represent standard error in this plot to normalize for differences in the number of data points collected with the standard- and high-load cells. The hardness of the four $REPO_4$ ceramics remained constant with depth from 100 nm through at least 1700 nm, which encompasses the 1500 nm-maximum depths in Ref. [5]. From Fig. 7, the hardness of $GdPO_4$ at 1500 nm depth was 7.9 ± 0.5 GPa, which is slightly higher than the 6.0 GPa reported by Hay et al. [5] The hardnesses of $TbPO_4$ (5.7 ± 0.9 GPa) and $DyPO_4$ (6.6 ± 0.5 GPa) were much higher than the 0.9 GPa and 3.2 GPa reported for $TbPO_4$ and $DyPO_4$ [5], respectively. Like elastic modulus, hardness is also quite sensitive to porosity, thus the discrepancy of hardness between the two studies may result from density differences.

While there was no significant strain-rate dependence in terms of the frequency of behaviors like elbows and pop-outs in the four $REPO_4$ compositions, we verified that strain-rate independence manifested in hardness measurements as well. The strain rate sensitivity exponent, m (Eq. (4)), is a measure of how the strength of a material varies with rate [37]. In terms of hardness, H, the strain rate sensitivity exponent is

$$m = \frac{\partial lnH}{\partial ln\dot{\varepsilon}} \tag{4}$$

where $\dot{\varepsilon}$ is the strain rate. In indentation tests with a constant loading rate, an equivalent strain rate, $\dot{\varepsilon} = \frac{1}{h}\frac{dh}{dt}$ [38], is derived from the loading rate, $\dot{P}$, and the peak load, P_{max} [39], yielding

$$\dot{\varepsilon} = \frac{\dot{P}}{2P_{max}} \quad , \tag{5}$$

though strain and strain rates are non-uniform strain and vary with time.

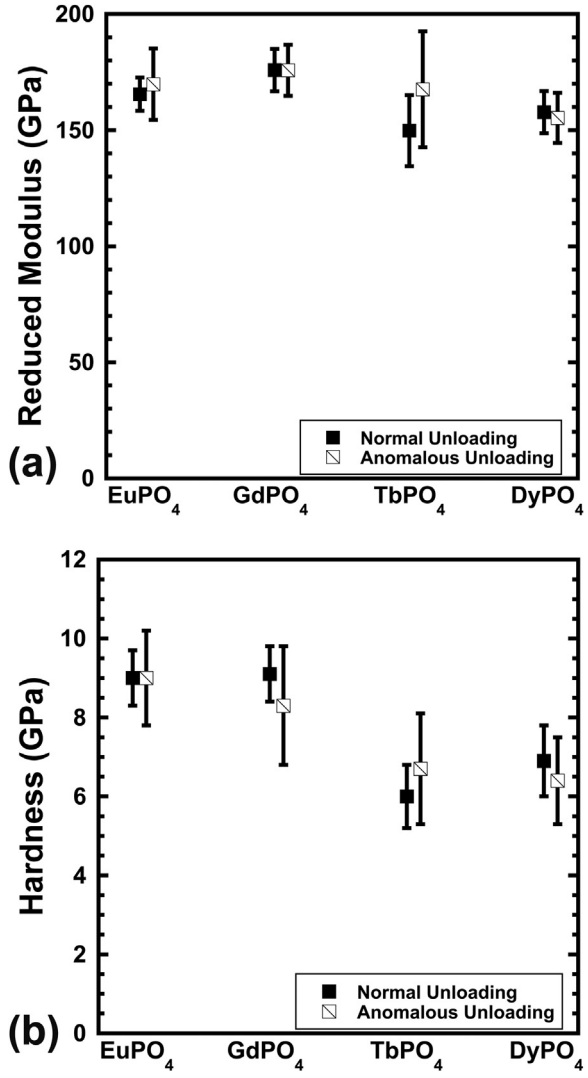

Fig. 5. Reduced modulus (a) and hardness (b) for elemental $REPO_4$. Data points represent average values and error bars represent standard deviation. Anomalous unloading includes pop-outs and elbows.

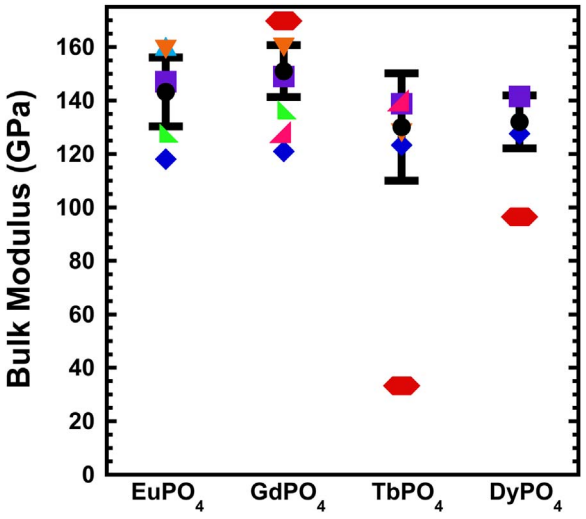

Fig. 6. Comparison of $REPO_4$s by bulk modulus. The values collected during this study are represented by • and show error bars indicating standard deviation for the values. The other symbols are representative of the following references, ■ =Li et al. [11], ◆=Kowalski *et al.* [12], ▲=Perriere et al. [10], ◣=Du et al. [7], ▼=Lacomba-Perales et al. [9], ◢=Heffernan et al. [8], and ⬣=Hay et al. [5].

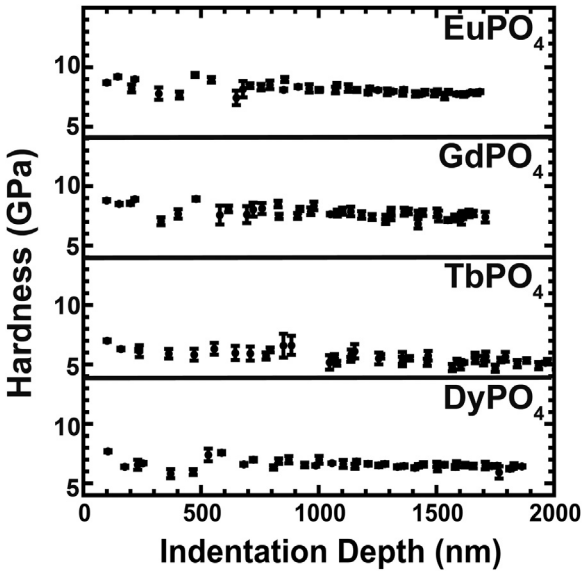

Fig. 7. Hardness is relatively constant with indentation depth. Error bars represent standard error.

The measured hardness of the four $REPO_4$s were plotted against the equivalent strain rates in log-log scale, as shown in Fig. 8. The m-value for each material was extracted from the slope of the linear fitting of the hardness data, from Eq. (4). The measured m-values for these $REPO_4$s range from 0.004 to 0.016, all of which are smaller than the m-values of phosphate glasses (m is around 0.020) [40], which were not considered strain-rate sensitive [41]. Therefore, the hardness of the four $REPO_4$ ceramics tested here were quite insensitive to strain rate, and differences in strain rate were unlikely to cause variation in hardness with different testing conditions.

4. Conclusions

This study characterized the mechanical behavior and properties of four $REPO_4$ materials ($EuPO_4$, $GdPO_4$, $TbPO_4$, and $DyPO_4$) near the monazite/xenotime boundary using nanoindentation. *In situ* nanoindentation within an SEM allowed for pop-ins to be correlated with the evolution of surface features such as cracks. Elbows and pop-outs were found to occur in both pressure-induced phase-transforming xenotime compositions as well as non-transforming monazite compositions, suggesting that this mechanical behavior cannot be used as a specific identifier of phase transformations within the class of $REPO_4$ materials. Furthermore, the frequency of elbow-type unloading behavior was independent of loading rate, consistent with a deformation process with a large activation volume such as twinning. The presence of elbows or pop-outs in the unloading data did not impact the measured reduced elastic modulus, which was found to be consistent with modulus values obtained by a variety of other techniques. Hardnesses for all four materials exceeded 5 GPa and were not impacted by strain rate or indentation depth over a wide range of testing conditions.

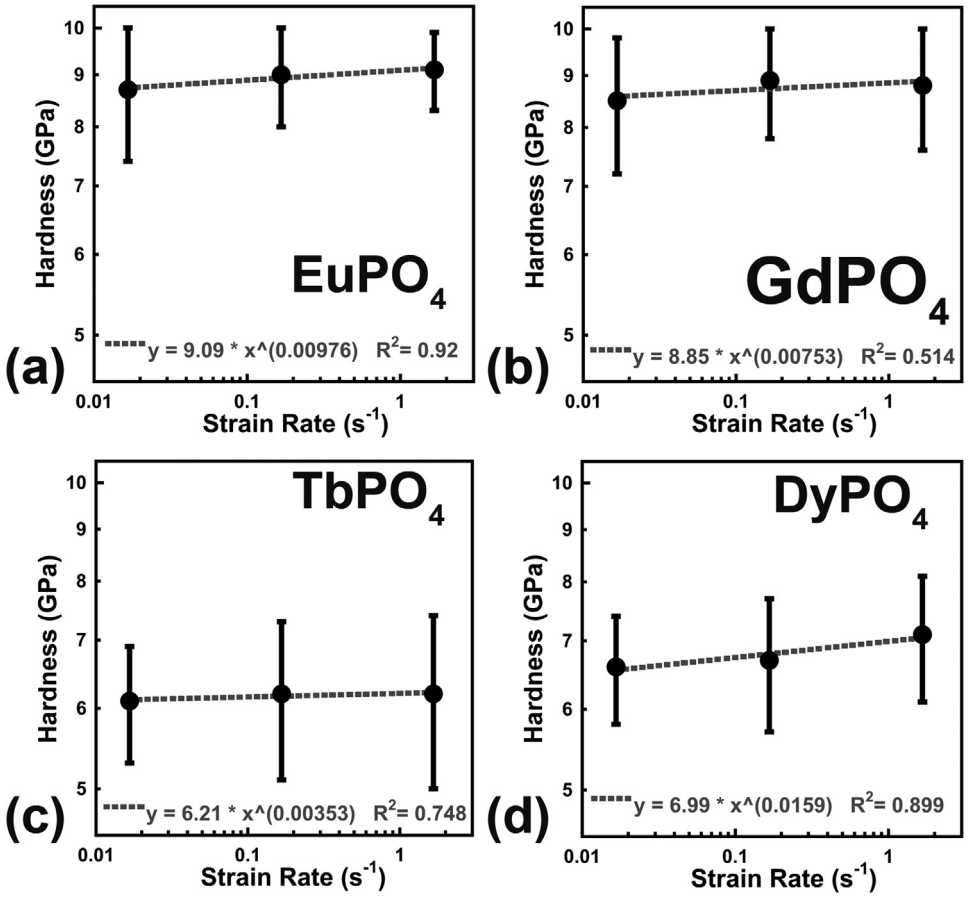

Fig. 8. Hardness as a function of equivalent strain rate for $EuPO_4$ (a), $GdPO_4$ (b), $TbPO_4$ (c), and $DyPO_4$ (d). Error bars represent standard deviation.

Acknowledgments

The researchers wish to acknowledge Aaron Miller for help in processing the hot pressed $TbPO_4$ pellet and the contributions of Zachary McMullen in the synthesis, processing, and sample preparation of the $EuPO_4$, $GdPO_4$, and $DyPO_4$. The researchers also wish to acknowledge the Virginia Ferguson Research Group at the University of Colorado, Boulder for use of their high load indentation cell. *In situ* nanoindentation were completed through an awarded user proposal: U2015B0008 at the Center for Integrated Nanotechnology at Los Alamos National Laboratory. This work was performed, in part, at the Center for Integrated Nanotechnologies, an Office of Science User Facility operated for the U.S. Department of Energy (DOE) Office of Science. Los Alamos National Laboratory, an affirmative action equal opportunity employer, is operated by Los Alamos National Security, LLC, for the National Nuclear Security Administration of the U.S. Department of Energy under contract DE-AC52-06NA25396. This research was funded by the National Science Foundation (NSF) under Award No.: DMR-1352499.

Appendix A. Supplementary material

Supplementary data associated with this article can be found in the online version at doi:10.1016/j.msea.2017.03.041.

References

[1] E.E. Boakye, P. Mogilevsky, R.S. Hay, G.E. Fair, Synthesis and phase composition of lanthanide phosphate nanoparticles $LnPO_4$(Ln"La, Gd, Tb, Dy, Y) and solid solutions for fiber coatings, J. Am. Ceram. Soc. 91 (12) (2008) 3841–3849.
[2] L.A. Boatner, Synthesis, structure, and properties of monazite, pretulite, and xenotime, Rev. Mineral. Geochem. 48 (1) (2002) 87–121.
[3] J.B. Davis, R.S. Hay, D.B. Marshall, P.E. Morgan, A. Sayir, Influence of Interfacial Roughness on Fiber Sliding in Oxide Composites with La-Monazite Interphases, J. Am. Ceram. Soc. 86 (2) (2003) 305–316.
[4] R.S. Hay, E.E. Boakye, P. Mogilevsky, G.E. Fair, T.A. Parthasarathy, J.E. Davis, Transformation plasticity in $(Gd_xDy_{1-x})PO_4$ fiber coatings during fiber push out, J. Eur. Ceram. Soc. 96 (5) (2013) 1586–1595.
[5] R.S. Hay, E.E. Boakye, P. Mogilevsky, Transformation plasticity in $TbPO_4$ and (Gd,Dy)PO_4 orthophosphates during indentation of polycrystalline specimens, J. Eur. Ceram. Soc. 34 (3) (2014) 773–781.
[6] R.S. Hay, P. Mogilevsky, E. Boakye, Phase transformations in xenotime rare-earth orthophosphates, Acta Mater. 61 (18) (2013) 6933–6947.
[7] A. Du, C. Wan, Z. Qu, W. Pan, Thermal conductivity of monazite-type REPO4 (RE=La, Ce, Nd, Sm, Eu, Gd), J. Am. Ceram. Soc. 92 (11) (2009) 2687–2692.
[8] K.M. Heffernan, N.L. Ross, E.C. Spencer, L.A. Boatner, The structural response of gadolinium phosphate to pressure, J. Solid State Chem. 241 (2016) 180–186.
[9] R. Lacomba-Perales, D. Errandonea, Y. Meng, M. Bettinelli, High-pressure stability and compressibility of APO_4 (A=La, Nd, Eu, Gd, Er, and Y) orthophosphates: an X-ray diffraction study using synchrotron radiation, Phys. Rev. B 81 (6) (2010) 064113.
[10] L. Perriere, D. Bregiroux, B. Naitali, E. Audubert, E. Champion, D.S. Smith, D. Bernache-Assollant, Microstructural dependence of the thermal and mechanical properties of monazite $LnPO_4$ (Ln=La to Gd), J. Eur. Ceram. Soc. 27 (10) (2007) 3207–3213.
[11] H. Li, S. Zhang, S. Zhou, X. Cao, Bonding characteristics, thermal expansibility, and compressibility of RXO4 (R= rare earths, X=P, as) within monazite and zircon structures, Inorg. Chem. 48 (10) (2009) 4542–4548.
[12] P.M. Kowalski, Y. Li, Relationship between the thermodynamic excess properties of mixing and the elastic moduli in the monazite-type ceramics, J. Eur. Ceram. Soc. 36 (8) (2016) 2093–2096.
[13] J. Feng, B. Xiao, R. Zhou, W. Pan, Anisotropy in elasticity and thermal conductivity of monazite-type $REPO_4$ (RE=La, Ce, Nd, Sm, Eu and Gd) from first-principles calculations, Acta Mater. 61 (19) (2013) 7364–7383.
[14] J.I. Jang, M.J. Lance, S.Q. Wen, T.Y. Tsui, G.M. Pharr, Indentation-induced phase transformations in silicon: influences of load, rate and indenter angle on the transformation behavior, Acta Mater. 53 (6) (2005) 1759–1770.
[15] B. Haberl, J.E. Bradby, S. Ruffell, J.S. Williams, P. Munroe, Phase transformations induced by spherical indentation in ion-implanted amorphous silicon, J. Appl. Phys. 100 (1) (2006).
[16] C.P. Frick, T.W. Lang, K. Spark, K. Gall, Stress-induced martensitic transformations and shape memory at nanometer scales, Acta Mater. 54 (8) (2006) 2223–2234.

[17] S. Rajagopalan, A.L. Little, M.A.M. Bourke, R. Vaidyanathan, Elastic modulus of shape-memory NiTi from in situ neutron diffraction during macroscopic loading, instrumented indentation, and extensometry, Appl. Phys. Lett. 86 (8) (2005).
[18] T.M. Wilkinson, M.A. Musselman, L.A. Boatner, D.R. Diercks, C.E. Packard, Indentation recovery in $GdPO_4$ and observation of deformation twinning, AIP Adv. 6 (9) (2016) 095029.
[19] D.X. Shi, D. Winslow, Accuracy of a volume fraction measurement using areal image-analysis, J. Test. Eval. 19 (3) (1991) 210–213.
[20] Y.X. Ni, J.M. Hughes, A.N. Mariano, Crystal-chemistry of the monazite and xenotime structures, Am. Mineral. 80 (1–2) (1995) 21–26.
[21] W.C. Oliver, G.M. Pharr, Improved technique for determining hardness and elastic modulus using load and displacement sensing indentation experiments, J. Mater. Res. 7 (6) (1992) 1564–1583.
[22] R.F. Cook, G.M. Pharr, Direct observation and analysis of indentation cracking in glasses and ceramics, J. Am. Ceram. Soc. 73 (4) (1990) 787–817.
[23] D.J. Oliver, B.R. Lawn, R.F. Cook, M.G. Reitsma, J.E. Bradby, J.S. Williams, P. Munroe, Giant pop-ins in nanoindented silicon and germanium caused by lateral cracking, J. Mater. Res. 23 (2) (2008) 297–301.
[24] A.C. Lund, A.M. Hodge, C.A. Schuh, Incipient plasticity during nanoindentation at elevated temperatures, Appl. Phys. Lett. 85 (8) (2004) 1362–1364.
[25] S.V. Hainsworth, T.F. Page, Nanoindentation studies of the chemomechanical effect in sapphire, J. Mater. Sci. 29 (21) (1994) 5529–5540.
[26] Y. Gaillard, C. Tromas, J. Woirgard, Quantitative analysis of dislocation pile-ups nucleated during nanoindentation in MgO, Acta Mater. 54 (5) (2006) 1409–1417.
[27] J. Ye, R.K. Mishra, A.R. Pelton, A.M. Minor, Direct observation of the NiTi martensitic phase transformation in nanoscale volumes, Acta Mater. 58 (2) (2010) 490–498.
[28] A. Tatsi, E. Stavrou, Y. Boulmetis, A. Kontos, Y. Raptis, C. Raptis, Raman study of tetragonal $TbPO_4$ and observation of a first-order phase transition at high pressure, J. Phys. Condens. Mat. 20 (42) (2008) 425216.
[29] A.G. Evans, A.H. Heuer, Transformation toughening in ceramics – martensitic transformations in crack-tip stress-fields, J. Am. Ceram. Soc. 63 (5–6) (1980) 241–248.
[30] P. Mogilevsky, T.A. Parthasarathy, Anisotropy in room temperature microhardness and indentation fracture of xenotime, Mater. Sci. Eng. A-Struct. 454 (2007) 227–238.
[31] T.M. Erickson, A.J. Cavosie, D.E. Moser, I.R. Barker, H.A. Radovan, Correlating planar microstructures in shocked zircon from the Vredefort Dome at multiple scales: crystallographic modeling, external and internal imaging, and EBSD structural analysis, Am. Mineral. 98 (1) (2013) 53–65.
[32] D. Ghosh, G. Subhash, N. Orlovskaya, Slip-line spacing in ZrB_2-based ultrahigh-temperature ceramics, Scr. Mater. 62 (11) (2010) 839–842.
[33] L. Huang, W. Yao, A.K. Mukherjee, J.M. Schoenung, Improved mechanical behavior and plastic deformation capability of ultrafine grain alumina ceramics, J. Am. Ceram. Soc. 95 (1) (2012) 379–385.
[34] Y. Hikichi, T. Ota, K. Daimon, T. Hattori, M. Mizuno, Thermal, mechanical, and chemical properties of sintered xenotime-type RPO4 (*R* =Y, Er, Yb, or Lu), J. Am. Ceram. Soc. 81 (8) (1998) 2216–2218.
[35] D.H. Kuo, W.M. Kriven, Characterization of yttrium phosphate and a yttrium phosphate/yttrium aluminate laminate, J. Am. Ceram. Soc. 78 (11) (1995) 3121–3124.
[36] N. Fleck, H. Otoyo, A. Needleman, Indentation of porous solids, Int. J. Solids Struct. 29 (13) (1992) 1613–1636.
[37] Q. Wei, Strain rate effects in the ultrafine grain and nanocrystalline regimes—influence on some constitutive responses, J. Mater. Sci. 42 (5) (2007) 1709–1727.
[38] A.C. Fischer-Cripps, Nanoindentation, 2nd ed, Springer, New York, 2002.
[39] D. Pan, M.W. Chen, Rate-change instrumented indentation for measuring strain rate sensitivity, J. Mater. Res. 24 (4) (2011) 1466–1470.
[40] R. Limbach, B.P. Rodrigues, L. Wondraczek, Strain-rate sensitivity of glasses, J. Non-Cryst. Solids 404 (2014) 124–134.
[41] R. Sujith, R. Kumar, Room temperature strain rate sensitivity in precursor derived HfO_2/Si-C-N(O) ceramic nanocomposites, AIP Adv. 4 (1) (2014) 017129.